



Facile synthesis of SnS nanostructures with different morphologies for supercapacitor and dye-sensitized solar cell applications

Mohd Arif Dar^{1,*} , D. Govindarajan¹, and Gulam Nabi Dar²

¹Department of Physics, Annamalai University, Annamalainagar, Chidambaram 608001, India

²Department of Physics, University of Kashmir, Srinagar, Jammu and Kashmir, India

Received: 1 March 2021

Accepted: 1 July 2021

Published online:

15 July 2021

© The Author(s), under exclusive licence to Springer Science+Business Media, LLC, part of Springer Nature 2021

ABSTRACT

In this paper, tin Sulfide (SnS) nanoparticles are synthesized with three different solvents through hydrothermal method and characterized by using X-ray diffraction, scanning electron microscopy, UV-DRS spectroscopy, Fourier transform infrared spectroscopy, energy-dispersive X-ray spectrum, supercapacitor, and photovoltaic performance. XRD patterns indicate that the prepared SnS nanoparticles exist in the orthorhombic phase. The SEM analysis clearly picturizes the morphological changes in the SnS nanoparticles synthesized through different solvents. The UV-DRS spectrum gives direct energy band gap which lies between 1.0 and 2.0 eV. The FT-IR spectrum explains various functional groups present in the SnS nanoparticles. The prepared SnS counter electrodes (CEs) showed good electrocatalytic activity in the redox reaction of the I^-/I_3^- . The efficiency of tin sulfide prepared in ethanol (SnS-e), tin sulfide prepared in acetone (SnS-a), and tin sulfide prepared in methanol (SnS-m) counter electrodes (CEs) are 9.99%, 9.90%, and 9.86% in Dye-sensitized solar cells (DSSC) than that of platinum counter electrode which is 9.80%. The specific capacitance of 284 F/g is obtained for SnS-e electrode at a current density of 5 A/g and an energy density of 216 Wh/kg corresponding to power density value of 1.6 KWh/kg which proves SnS-e electrode possesses better capacitive performance than SnS-a and SnS-m electrodes, respectively.

1 Introduction

In recent years, nanostructured semiconductors have attracted greater interest due to their significant applications in electronic, optical, and superconductor devices [1–3]. The key properties of these

nanostructured materials rely upon their designs including morphology, geometry, and hierarchical structures [4]. Currently, scientists have made much effort to develop novel techniques to synthesize nanostructured metal chalcogenide semiconductors such as GeSe, GeS, SnS, SnSe, PbSe, and PbS due to

Address correspondence to E-mail: dararifphy@gmail.com

their various potential applications like infrared sensors, photo transducers, optical, and photovoltaic properties [5–7]. Among these chalcogenide semiconductors, SnS has got greater research interest because of its layered structure, narrow band gap, high absorption coefficient in the visible region, chemical stability, carrier mobility, and p-type electrical conductivity [8]. The layered structure in tin sulfides effectively promotes the intercalation of ions during electrochemical reactions and makes them more favorable and alternative anodic material for supercapacitor applications [9].

Further, different materials have been used for the supercapacitor applications such as carbonaceous materials [10], metallic materials [11], and conjugated organo-polymers [12]. Carbon-based materials, with long cycling stability and high electrical conductivity, fall under the category of electrical double-layer capacitor, whereas the other two types of materials store energy in a Faradaic or redox-type process similar to batteries, which gives high energy density and fall under the category of pseudocapacitor. Recently, metal sulfides such as SnS have emerged as one of the most potential candidates for energy storage application. Both physical (electrical conductivity, mechanical, and thermal stability) and chemical (redox chemistry) properties contribute to high specific capacitance and make them suitable as the electrode material for lithium-ion battery and supercapacitor applications [13]. Apart from this, different transition metal sulfides such as NiS, CoS, WS, MoS₂, SnS, and SnS₂ have also found application in DSSCs as CEs. Among these, SnS is found to have significant efficiency in DSSCs as CEs and has become a promising material for CEs in DSSCs.

Different methods have been employed for the synthesization of SnS nanostructures like Bridgman method, solid-state reaction method, solid-state metathesis method, brush platinum technique, and self-propagating high-temperature synthesis [14–16]. But these methods possess some important limitations, i.e., need of special devices, high processing temperature, and requirements of toxic reagents. Recently, some solution-based methods have been reported such as solvothermal, hydrothermal, and organometallic methods for the preparation of SnS nanostructures with different morphologies like nanorods, nanoflowers, dendrite-like nanoparticles, nanosheets, belt-like nanocrystals, nanowires

through hydro/solvothermal methods, and enhancing its electrical and optical properties [12–18].

In this study, SnS nanospheres are synthesized by simple, surfactant-free solvothermal method using ethanol, methanol, and acetone as solvents. The final product was characterized using XRD, FT-IR, UV-DRS, SEM, EDX, and TEM techniques. The prepared SnS-e, SnS-a, and SnS-m electrodes are examined for photovoltaic and electrochemical performances.

2 Experimental procedure

2.1 Materials and methods

The chemicals used for the synthesis of SnS nanoparticles are tin (II) chloride (SnCl₂·2H₂O, Sigma-Aldrich 98% purity), Thioacetamide (Sigma-Aldrich 99% purity), and Acetic acid (HPLC company Ltd. India, 99.7% purity). All other solvents used were purchased from Loba Chemical limited, India.

For synthesization, 0.1 mmol of SnCl₂·2H₂O was dissolved in 5 ml of acetic acid with constant stirring at room temperature. After 5 min, 50 ml of ethanol plus 0.75 g of TAA is added to the solution. After all the precursors are dissolved and a homogeneous solution is formed, the solution was transferred to a Teflon-lined stainless steel autoclave and heated in an electric oven at 200 °C for 24 h. The obtained yellow color precipitates were washed with distilled water several times so that all the impurities are removed and dried in a hot electric oven for 10 h at 60 °C temperature. Finally, the obtained product was grounded with the help of agate mortar and pestles and named as SnS-e. The same procedure is repeated for other solvents such as methanol and acetone and the final product is named as SnS-m and SnS-a, respectively. The schematic representation of the formation mechanism of SnS nanospheres is shown in Fig. 1.

2.2 Synthesis of SnS hybrid CEs

The obtained yellow color SnS material was dispersed in hexamethylene with a concentration of 0.08 gml⁻¹ to form SnS hybrid ink. Three different SnS-e, SnS-m, and SnS-a hybrid CEs were fabricated by directly drop-casting the ink on the cleaned FTO glass and dried at room temperature.

2.3 Fabrication of DSSCs

For fabrication, 0.5 mM of N719 Di-tetrabutylammonium cis-bis (isothiocyanato) bis (2,2'-bipyridyl-4,4'-dicarboxylato)-ruthenium(II) solution was prepared with ethanol. Then the sintered TiO_2 films were dispersed into the above N719 ethanol solution at 70 °C for 12 h. The sensitized TiO_2 films were washed with ethanol to obtain TiO_2 photoanode. The TiO_2 photoanode was placed on a light-blocking mask and clamped with the as-synthesized CEs. The open devices were obtained by injecting the liquid electrolytes into the gap between the TiO_2 photoanode and SnS-e, SnS-m, and SnS-a CEs. The photoactive area of DSSCs was measured to be 0.25 cm².

2.4 Materials characterizations

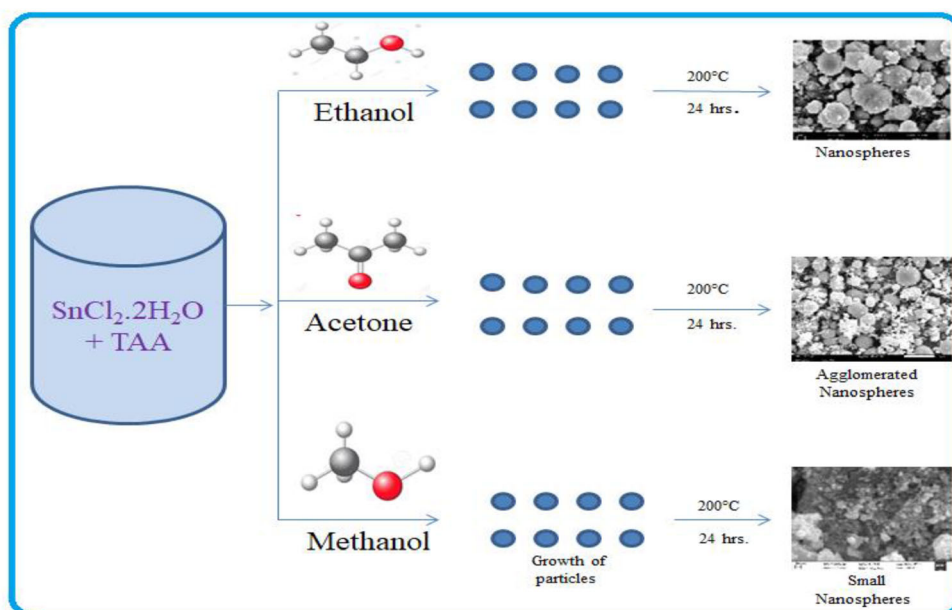
The crystallinity and phase formation of synthesized SnS nanoparticles were analyzed with the help of (Panalytical diffractometer—XPERT3) CuK_α radiation of 1.5 nm wavelength. XRD peaks were recorded at a scan rate of 0.04 min⁻¹ in the range 0 to 80°. The morphology of the samples was analyzed using SEM (JEOL-JSM-IT200) and EDAX (JEOL-JSM-IT200). The UV-Vis Drs spectra were recorded on a Shimadzu UV1800 and for FT-IR spectra Thermo Nicolet 380 spectrophotometer was utilized. Cyclic voltammetry

(CV) was recorded in a three-electrode system in an acetonitrile solution (mixture of 10 mM LiI, 0.1 mM LiClO_4 , and 1 mM I_2) at a scanning rate of 50 mV/s by using a BAS100 B/W electrochemical analyzer. Pt acted as a counter electrode and the Ag/Ag^+ acted as a reference electrode. Solar energy conversion efficiency (SECE) was measured using a solar simulator (94063A, Newport Stratford Inc.) under 1 sun illumination (100 mWcm⁻²) with a sample area of 0.25 cm².

2.5 Electrochemical measurements

The electrochemical measurements of SnS nanoparticles were carried out by using three-electrode system using Ag/AgCl electrode as reference, platinum electrode as a counter, and Nickel foil with a mixture of active material as working electrode, respectively. The working electrode was made up of SnS material, PVDF, and acetylene black with a mass ratio of 80:10:10 mixed in Glutaraldehyde solution. The slurry formed was coated on Nickel strip (2.0 × 1.0 cm) and then dried at 100 °C for 12 h. All electrochemical measurements were carried out at room temperature using an Autolab (PGSTAT101) Metrohm, Switzerland, Electrochemical Workstation, in a 3 M KOH aqueous solution as electrolyte.

Fig. 1 Schematic representation of the formation mechanism of SnS nanospheres



3 Results and discussions

3.1 Structural analysis

XRD results of SnS-e, SnS-m, and SnS-a nanoparticles are shown in Fig. 2. As seen from the XRD spectrum, it is confirmed that the SnS nanoparticles are formed of single-phase polycrystalline structure and are indexed as (110), (121), (021), (101), (111), (131), (141), (002), (211), (151), (160), (061), (041), (251), and (080) planes for the angular positions at 22.03°, 26.03°, 27.45°, 30.49°, 31.54°, 39.06°, 44.75°, 45.51°, 48.60°, 51.34°, 53.34°, 56.62°, 64.24°, and 66.80°, respectively (JCPDS card no.39–0354). XRD pattern does not show any unwanted phase corresponding to any structure confirming the purity of the products. These entire diffraction peaks match with the peaks observed in the previous report of Masoud et al. [19].

X-ray diffraction peak gets broadened in the nanocrystals due to the intrinsic strain effect as well as due to crystallite size effect and this peak broadening normally consists of two parts instrumental broadening and physical broadening [20, 21]. The corrected instrumental broadening is given by the relation [22]

$$(\beta_D)^2 = (\beta_m)^2 - (\beta_i)^2, \tag{1}$$

where β_m is the measured broadening, β_i is the instrumental broadening, and β_D is the corrected broadening. The physical broadening and instrumental broadening of the sample are measured as

FWHM. Using the corrected physical broadening, the average crystallite size can be calculated with the help of the Scherrer equation given as [23]

$$D = \frac{K\lambda}{\beta \cos \theta} = \frac{0.9\lambda}{\beta \cos \theta}, \tag{2}$$

where λ is the Wavelength, β is the Full width half maximum, and θ is the Bragg's angle. The dislocation density was calculated by Williamson and Smallman's relation [24]:

$$\delta = \frac{n}{D^2} = \frac{1}{D^2}, \tag{3}$$

where n is equal to unity, D is the crystalline size. The microstrain in the samples was calculated using the relation [25]

$$\varepsilon = \frac{\beta \cos \theta}{4}. \tag{4}$$

The lattice parameters were calculated according to the relation [24]

$$\frac{1}{d_{hkl}^2} = \frac{h^2}{a^2} + \frac{k^2}{b^2} + \frac{l^2}{c^2}, \tag{5}$$

where d_{hkl} represents the interplanar spacing, hkl is the Miller indices. The X-ray density was calculated by using the relation [26]

$$P = \frac{ZM}{a^3 N_A}, \tag{6}$$

where Z represents number of atoms per unit cell, P is the Density (g/cm^3), a is the Edge length in cm, M is the Molar mass in g/mol , and N_A is the Avogadro's constant.

The calculated parameters from the XRD data are all listed in Table 1. It is observed that the crystalline size of the SnS-e, SnS-a, and SnS-m nanoparticles as 28 nm, 22 nm, and 19 nm, respectively.

Debye Scherrer formula considers only the effect of crystalline size on the XRD peak broadening, but it does not tell us about the intrinsic strain, which gets developed in the nanocrystals due to the grain boundary, point defect, stacking faults, and triple junction [27, 28]. To consider the effect of intrinsic strain, there are many methods such as Warren–Averbach method and Williamson–Hall method (W–H) which consider the effect of this intrinsic strain and can be used for the calculation of the intrinsic strain along with the crystallite size. Above all these methods, W–H method is a very easy and simplified one [29, 30]. According to W–H method, physical line

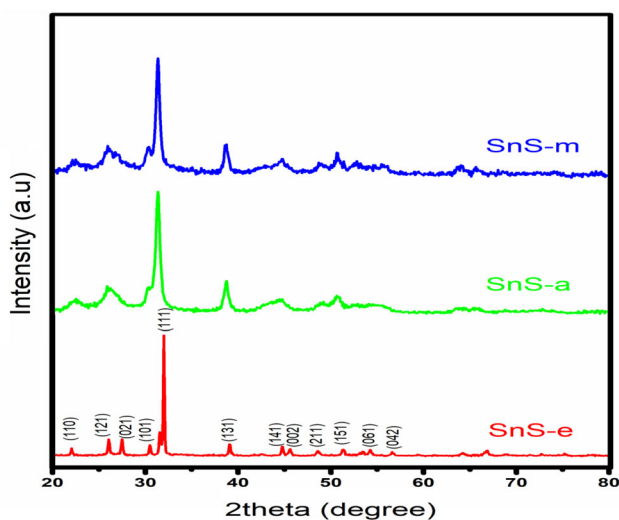


Fig. 2 XRD spectra of SnS-e, SnS-a, and SnS-m nanoparticles (Color figure online)

Table 1 Structural parameters of SnS-e, SnS-a, and SnS-m nanoparticles

Samples	Crystalline size D (nm)	Microstrain $\times 10^{-3}$	Dislocation density $\times 10^{15}$ (lines/ m^2)	Lattice parameters			Volume $V = abc$	Density g/cm^2	W–H method	
				a	b	c			D (nm)	$\varepsilon \times 10^{-3}$
SnS-e	28	1.5	2.0	4.31	11.20	3.98	192	5.21	34	2.0
SnS-a	22	2.1	5.3	4.27	11.13	3.94	188	5.34	29	2.5
SnS-m	19	2.1	5.1	4.30	10.92	3.96	186	5.38	20	2.2

broadening of X-ray diffraction peak occurs due to the size, microstrain of the nanocrystals, and the total broadening can be written as

$$\beta_{\text{total}} = \beta_{\text{size}} + \beta_{\text{strain}} \quad (7)$$

The intrinsic strain β_{strain} affects the physical broadening of the XRD profile and thus the strain-induced peak broadening can be expressed as [20]

$$\beta_{\text{strain}} = 4\varepsilon \cdot \tan \theta \quad (8)$$

So, the total broadening due to size and strain in a particular peak having the $[hkl]$ value can be expressed as

$$\beta_{[hkl]} = \beta_{\text{size}} + \beta_{\text{strain}} \quad (9)$$

where

$$\beta_{\text{size}} = \frac{K\lambda}{D \cos \theta} \quad (10)$$

Now Eq. (7) can be written as

$$\beta_{hkl} = \frac{K\lambda}{D \cos \theta} + 4\varepsilon \cdot \tan \theta \quad (11)$$

where β_{hkl} is the full width at half maximum peak intensity at different diffraction planes. On re-arranging Eq. (11), we can write

$$\beta_{hkl} \cos \theta = \frac{K\lambda}{D} + 4\varepsilon \cdot \sin \theta \quad (12)$$

Equation (12) is an equation of a straight line and is known as the uniform deformation model (UDM) equation, which considers the isotropic nature of the crystals. Figure 3 shows the plotting of this Eq. (12), with $4\sin\theta$ along x-axis and $\beta_{hkl} \cdot \cos\theta$ along with y-axis corresponding to each diffraction peak of SnS-e, SnS-a, and SnS-m nanoparticles. The slope of this straight line provides the value of the intrinsic strain, whereas the intercept gives the crystallite size of the SnS nanocrystals. The origin of the lattice strain is attributed mainly to the lattice contraction or lattice

expansion in the nanocrystals due to size confinement, because the atomic arrangement gets slightly modified due to size confinement, compared to their bulk counterpart. On the other hand, many defects also get created at the lattice structure due to the size confinement and this in turn results in the lattice strain. The crystallite sizes have been determined from the uniform deformation model (UDM) as 34 nm, 29 nm, and 20 nm, whereas the intrinsic strains are 2.0×10^{-3} , 2.5×10^{-3} , and 2.2×10^{-3} .

3.2 Raman analysis

Raman spectroscopy is one of the advanced techniques to examine the chemical states and compositions of nanoparticles. Figure 4 shows the Raman spectrum of the SnS-e, SnS-a, and SnS-m nanoparticles recorded at room temperature and it is clearly observed that there are three Raman peaks at 137 cm^{-1} , 192 cm^{-1} , and 278 cm^{-1} for SnS-e nanoparticles. The lattice vibration at 137 cm^{-1} corresponds to the B_{2u} mode, the small peak at 192 cm^{-1}

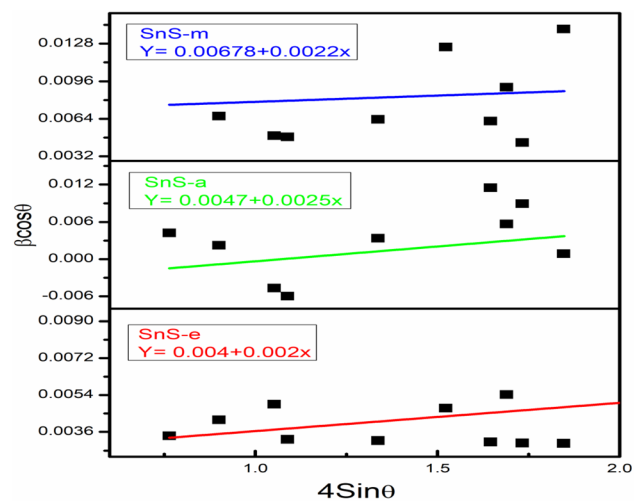


Fig. 3 UDM plot of SnS-e, SnS-a, and SnS-m nanoparticles (Color figure online)

is assigned to the A_g modes and the major high intensity peak at 278 cm^{-1} is assigned to B_{2g} mode of SnS, respectively [31]. The Raman peak observed at 280 cm^{-1} for SnS-a and SnS-m nanoparticles are assigned to $2A_g$ and the peak at 197 cm^{-1} for SnS-m nanoparticles corresponds to A_g modes, respectively. The peaks determined matched with the results observed by Gau et al. and Radik et al. [32, 33].

3.3 Optical properties

The optical property of synthesized SnS-e, SnS-a, and SnS-m nanoparticles was obtained through UV-DRS absorption spectrum (Fig. 5a) within the range of 200–800 nm where the absorption peaks are observed at 250 nm for SnS-e, 230 nm for SnS-a and SnS-m nanoparticles. The direct energy band gap values of synthesized SnS-e, SnS-a, and SnS-m nanoparticles were calculated with the help of Tauc and Davis–Mott model by extrapolating the linear region of the plot with the energy axis and the intersection value corresponds to the band gap energy [34].

$$\alpha h\nu = k(h\nu - E_g)^2, \quad (13)$$

where the symbol h is Plank's constant, ν is the frequency, and E_g is the energy band gap and α is the absorption coefficient and is defined by the Beer–Lambert law as follows:

$$\alpha = -\ln \frac{A}{L}, \quad (14)$$

where ' A ' is the absorbance and ' L ' is the optical path length. Figure 5b shows energy band gap values of

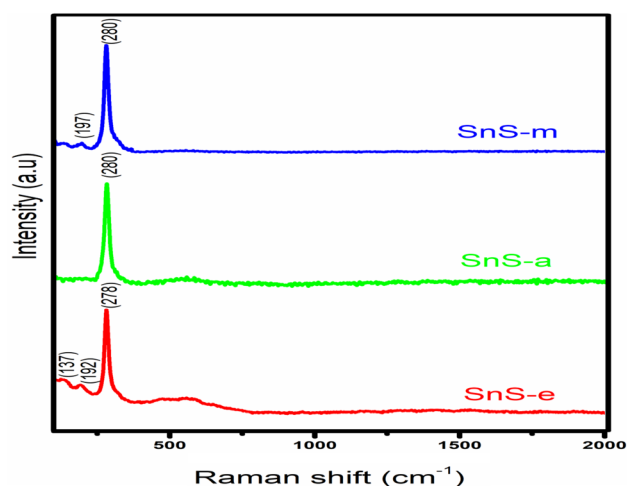


Fig. 4 Raman spectrum of SnS-e, SnS-a, and SnS-m nanoparticles (Color figure online)

the as-synthesized SnS-e, SnS-a, and SnS-m nanoparticles and it is observed that the energy band gap values are 1.5 eV, 1.9 eV, and 2.1 eV. The increase in direct band gap values of SnS-e, SnS-a, and SnS-m nanoparticles compared to the bulk SnS (1–1.3 eV) are due to the quantum confinement effect in the nano regime which arose from the small size of the particles as well as their morphologies [34].

3.4 FT-IR analysis

FT-IR spectra of SnS-e, SnS-a, and SnS-m nanoparticles are shown in Fig. 6. It is observed that the spectrum of SnS-e, SnS-a, and SnS-m nanoparticles shows the characteristic absorption peaks of SnS nanoparticles with different functional groups. The IR peaks observed in the spectra of SnS-e, SnS-a, and SnS-m nanoparticles are 469 cm^{-1} , 616 cm^{-1} , 620 cm^{-1} , 873 cm^{-1} , 1024 cm^{-1} , 1027 cm^{-1} , 1110 cm^{-1} , 1113 cm^{-1} , 1227 cm^{-1} , 1271 cm^{-1} , 1382 cm^{-1} , 1633 cm^{-1} , 2852 cm^{-1} , 2921 cm^{-1} , 3423 cm^{-1} , and 3432 cm^{-1} , respectively. The peaks observed at 469 cm^{-1} , 616 cm^{-1} , 620 cm^{-1} , 873 cm^{-1} are attributed to Sn–S stretching vibrations [35]. The peaks observed at 1024 cm^{-1} , 1027 cm^{-1} , 1113 cm^{-1} are attributed to C–O, and the peaks noted at 1227 cm^{-1} , 1271 cm^{-1} are attributed to C=C bonds in the SnS nanoparticles. The absorption band at 1382 cm^{-1} is attributed to C=O functional groups [36], the band at 2852 cm^{-1} , 2921 cm^{-1} corresponds to C–H stretching of an aldehyde, and the bands at 3423 cm^{-1} , 3432 cm^{-1} correspond to the (O–H) stretch of the hydroxyl group of various functional groups, such as aldehydes, alcohols, and acids [37].

3.5 Morphological analysis

Figure 7a–f represents the SEM images of SnS-e, SnS-a, and SnS-m nanoparticles. From these SEM images, it is clear that the effects of solvents and precursors play a significant role in the morphology of SnS nanoparticles. Figure 7a, b shows the clear spherical shapes of SnS-e nanoparticles in micrometer as well as in nanometer range. The SnS-a (Fig. 7c, d) and SnS-m (Fig. 7e, f) morphology also appeared as spheres which are small in size and agglomerated may be due to the solvent acetone and methanol used in these reactions. Thus, on the basis of present study, it is observed that the solvents and precursors play very

Fig. 5 **a** UV–Vis spectrum **b** direct band gap of SnS-e, SnS-a, and SnS-m nanoparticles (Color figure online)

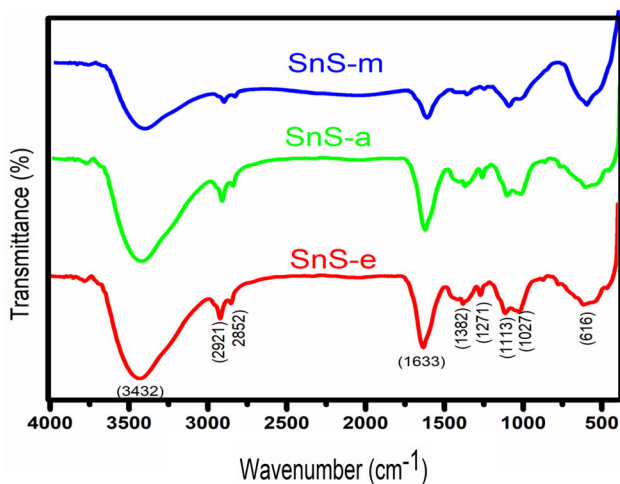
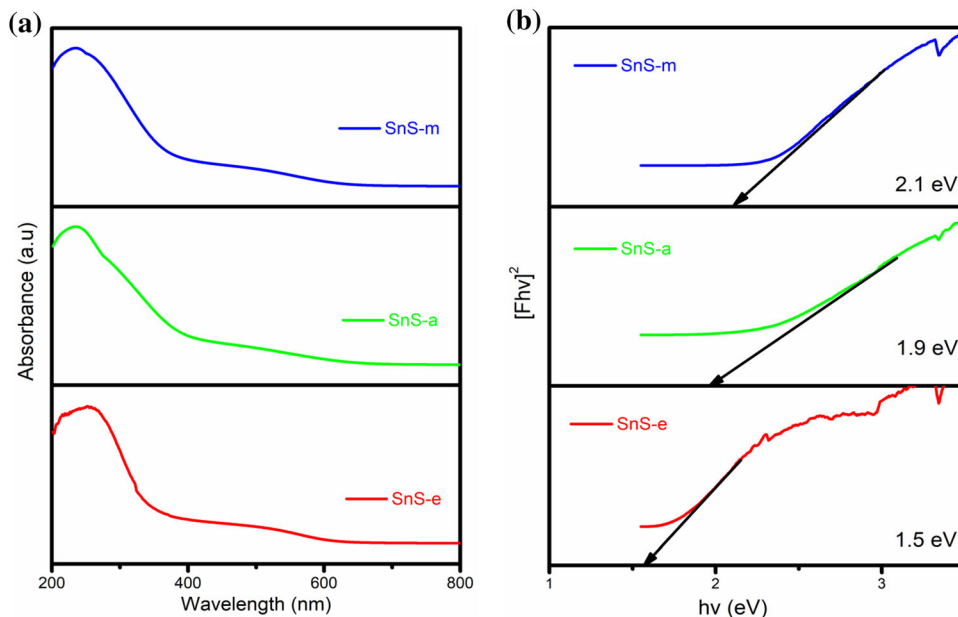


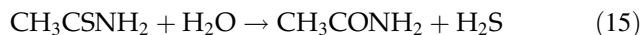
Fig. 6 FT-IR spectrum of SnS-e, SnS-a, and SnS-m nanoparticles (Color figure online)

important role in the construction of architectures of spherical like images of SnS nanoparticles.

Also, TEM analysis of SnS-e nanoparticles was carried out and shown in Fig. 8a, b. From these TEM images, it can be seen that SnS-e nanoparticles are spherical in shape and at higher magnification of SnS-e nanoparticle (Fig. 8c) shows the lattice fringes with the inter-planer spacing of 0.283 nm, which is revealed to (111) plane of orthorhombic crystal structure. The SAED pattern shows clear spot, which clearly understands the polycrystalline nature of SnS-e nanoparticles (Fig. 8d). From the TEM histogram (Fig. 9), the average particle size is calculated as

29 nm with the help of J-image software and matched with the crystallite size calculated from Scherer formula (Table 0.1).

Based on the SEM and TEM analyses, the formation of nanospheres can be explained by considering the various steps involved in the reaction. Previous reports and observations, the sulfur concentration, and different solvents played very important role in constructing different types of architectures of SnS nanoparticles [38]. In the beginning of the solvothermal reaction, Sn anions interact with acetic acid and form complex materials, whereas TAA decomposition leads to the formation of SnS. The reaction is as follows:



The precipitation of metal sulfides by thioacetamide can be explained in two different processes: one is the precipitation of metal sulfide by TAA at a low pH, and the other is the direct reaction of TAA with the metal precursor at a high pH [39, 40]. In our case, the presence of acetic acid used in the reaction certainly follows the first condition, in which the hydrolysis of TAA formed hydrogen sulfide (H_2S), which is followed by the formation of small SnS nuclei. These tiny nuclei grow and form a spherical nanostructure. These nanospheres are distinctly

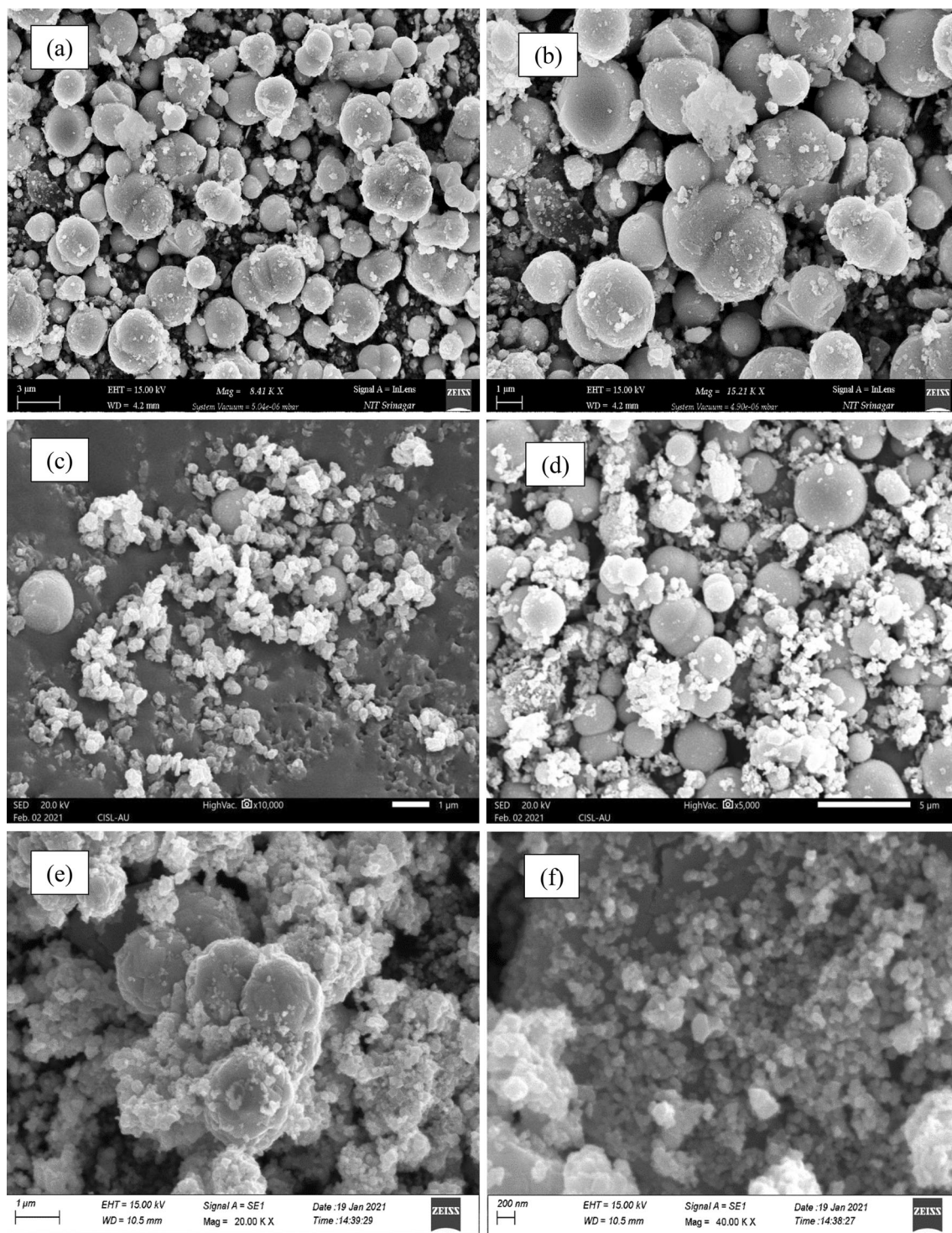


Fig. 7 a–f Shows SEM images of SnS-e, SnS-a, and SnS-m nanoparticles

visible in the case of ethanol as a solvent (SnS-e), whereas in the cases of acetone and methanol, the obtained are agglomerated.

3.6 Compositional analysis

Energy-dispersive X-ray spectroscopy (EDX) investigates subjective and quantitative analyses of components that might be involved with the formation of

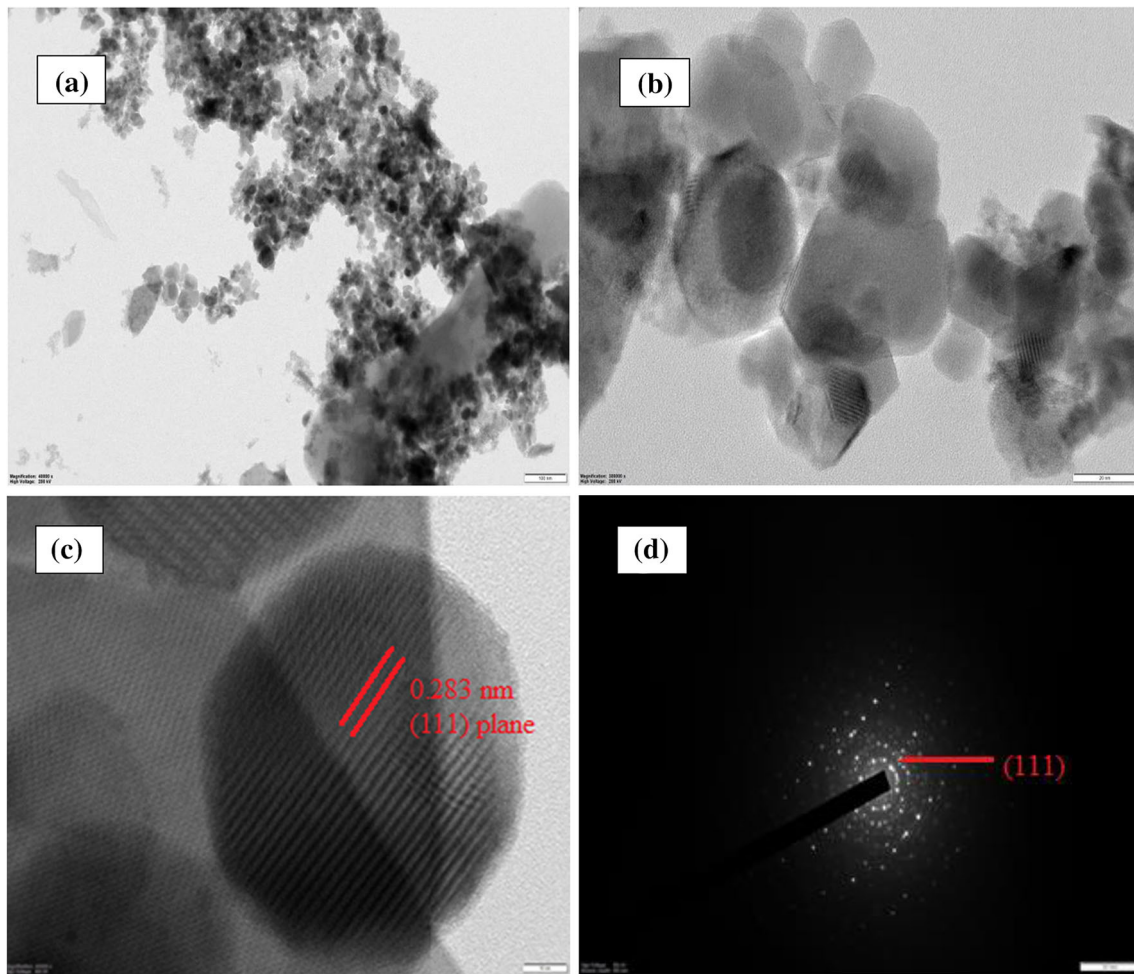


Fig. 8 a–d Shows TEM with SEAD pattern SnS-e nanoparticles

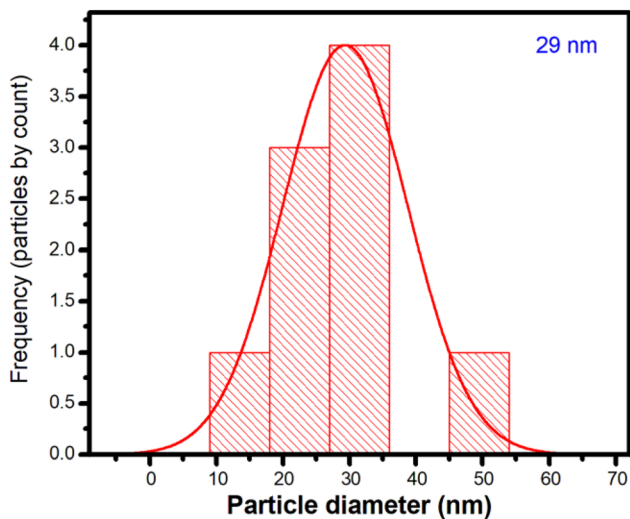


Fig. 9 Histogram of SnS-e nanoparticles

SnS-e nanoparticles. Figure 8a, b represents the elemental analysis of SnS-e nanoparticles, which confirms the presence of Sn and S elements and indicate the purity of the sample. Figure 8c shows the atomic mass percentage of the synthesized SnS-e nanoparticles. The EDX spectrum clearly picturizes the mass percentage of ‘Sn’ as 74.49 and ‘S’ as 25.51 that confirms the formation and purity of SnS-e nanoparticles. The mass and atomic percentage of elements present in the SnS-e nanoparticles are listed in the inset table in Fig. 10c.

3.7 Electrochemical properties

The capacitive performances of SnS-e, SnS-a, and SnS-m electrodes were examined by cyclic voltammetry and Galvanostatic charging/discharging techniques in 3 M of KOH electrolyte solution. Figure 11a–c represents the CV curves of SnS-e, SnS-

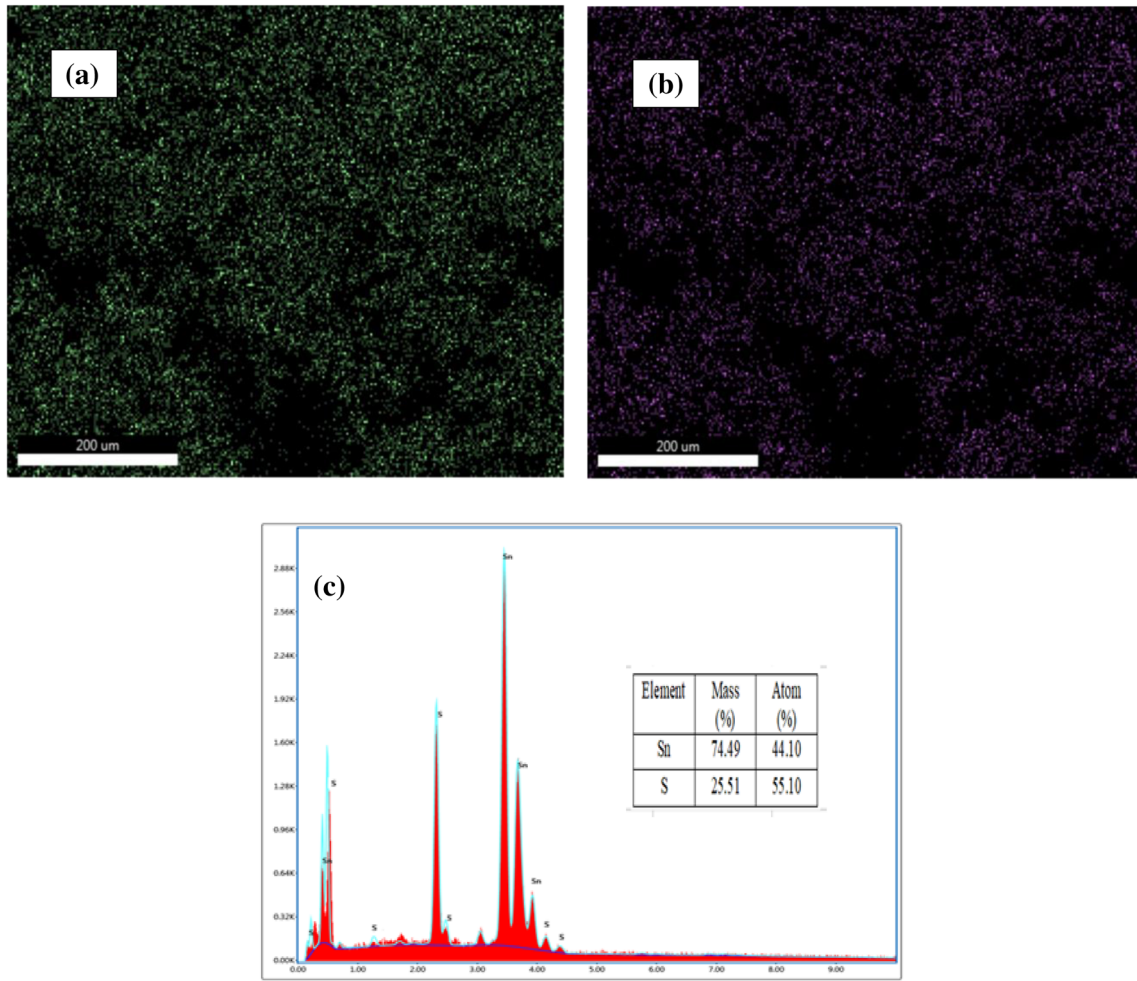


Fig. 10 a and b Elemental analysis of Sn and S c EDX spectrum of SnS-e nanoparticles

a, and SnS-m electrodes at different scan rates ranging from 10 to 100 mV/s within the potential window of -0.3 to 0.7 V. From these CV curves, the SnS-e, SnS-a, and SnS-m electrodes show quasi-rectangular shapes, which indicate EDLC nature of the SnS-e, SnS-a, and SnS-m electrodes. The area of CV curves increases from scan rate of 10–100 mv/s further signifying the capacitive behavior of SnS-e, SnS-a, and SnS-m electrodes. From the CV curves, the specific capacitance C_s is calculated by using equation [41].

$$C_s = \frac{1}{mk(v_f - v_i)} \int_{v_i}^{v_f} I(V)dv \tag{18}$$

$$C_s = \frac{S}{mk\Delta v}, \tag{19}$$

where S is the area enclosed by the CV curve, m is the mass, k is the specific capacitance, and Δv is the potential window. The calculated values of specific

capacitance are 2463 F/g, 1334 F/g, 957 F/g, 769 F/g, 656 F/g, and 410 F/g for SnS-e electrode; 1249 F/g, 649 F/g, 449 F/g, 349 F/g, 289 F/g, and 174 F/g for SnS-a electrode; and 749 F/g, 399 F/g, 283 F/g, 114 F/g, 189 F/g, and 124 F/g for SnS-m electrode at the scan rate of 10 mV/s, 20 mV/s, 30 mV/s, 40 mV/s, 50 mV/s, and 100 mV/s, respectively. Figure 11d represents the variation of specific capacitance verses scan rate and it is clearly observed that the values of specific capacitance are higher at lower scan rates as compared to higher scan rates which is due to the more time available to intercalate OH^- ions at lower scan rates than that of higher scan rates [42]. Moreover, the specific capacitance values of SnS-e electrode are higher than that of SnS-a and SnS-m electrodes.

The Galvanostatic charging/discharging of SnS-e, SnS-a, and SnS-m electrodes at a current density of 5 to 10 A/g having a potential window of -0.4 to

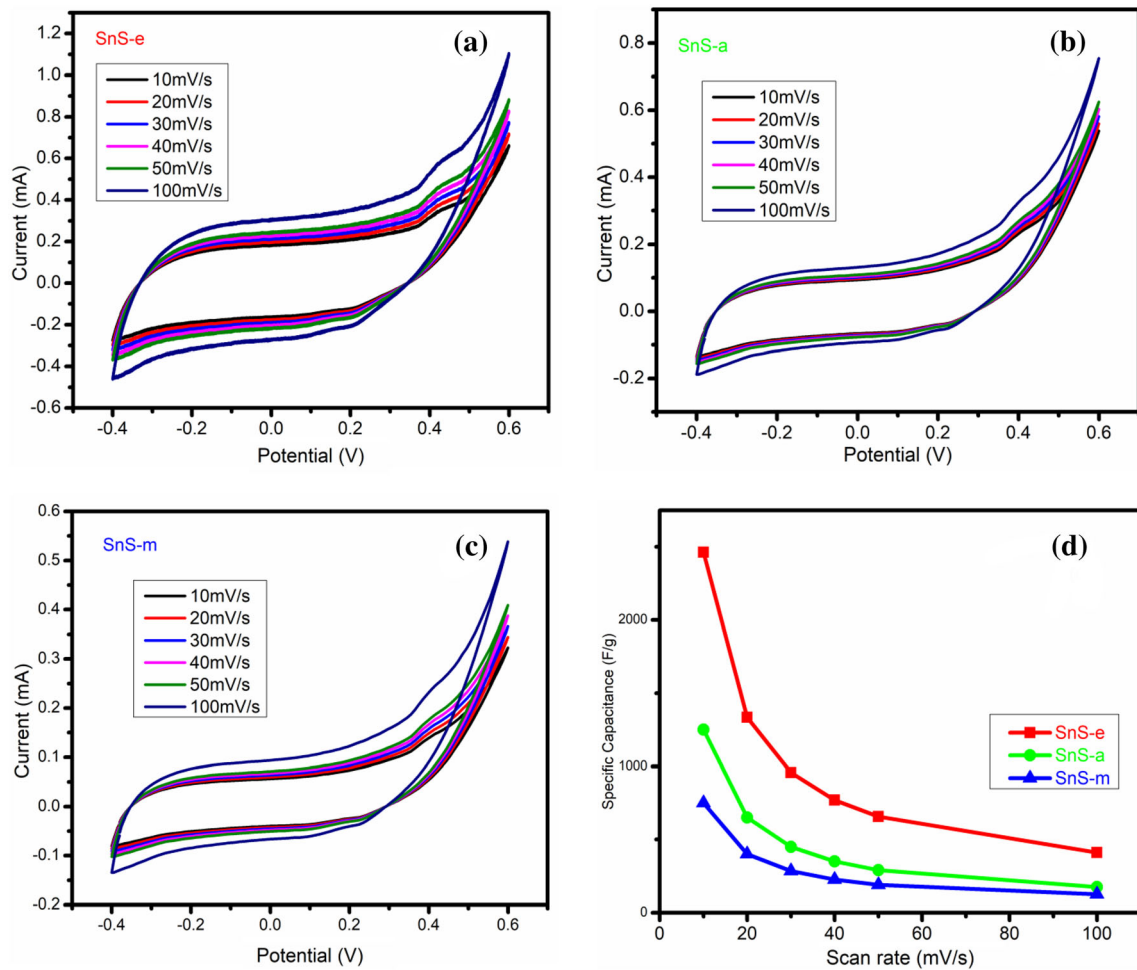


Fig. 11 a–c Cyclic voltammograms d Scan rate vs specific capacitance of SnS-e, SnS-a, and SnS-m electrodes (Color figure online)

0.4 V in 3 M of KOH electrolyte is shown in Fig. 12a–c. The specific capacitance of SnS-e, SnS-a, and SnS-m electrodes can be calculated by using the following expression [43, 44]:

$$C_p = \frac{I\Delta t}{m\Delta v}, \quad (20)$$

where I is the current density or discharge current, Δt is the discharge time, m is the mass, and Δv is the potential window. From GCD curves, the C_p values are 284 F/g, 230 F/g, 221 F/g, and 215 F/g for SnS-e electrode, 200 F/g, 185 F/g, 144 F/g, and 105 F/g for SnS-a electrode and 180 F/g, 155 F/g, 134 F/g, and 96 F/g for SnS-m electrode for the current density 5 A/g, 6 A/g, 8 A/g, and 10 A/g, respectively. Figure 12d shows us the variation of specific capacitance verses current density and it is clear that the specific capacitance values decrease at higher current densities which is due to the incremental voltage drop and

deficient active material being associated in the redox reaction [42]. Here in GCDs curves, the calculated values of specific capacitance are higher for SnS-e electrode as compared to the SnS-a and SnS-m electrodes, respectively.

The other important parameters such as energy density and powder density can be calculated by using the following expressions [45]:

$$E_d = \frac{1}{2}CV^2 \quad (21)$$

$$P_d = \frac{E}{t} \quad (22)$$

Here E_d is the energy density, C is the specific capacitance, V is the potential window, P_d is the powder density, and t is the discharging time. The calculated energy densities are 216 Wh/kg, 175 Wh/kg, 168 Wh/kg, and 163 Wh/kg for SnS-e electrode, 196 Wh/kg, 170 Wh/kg, 154 Wh/kg, and 134 Wh/kg

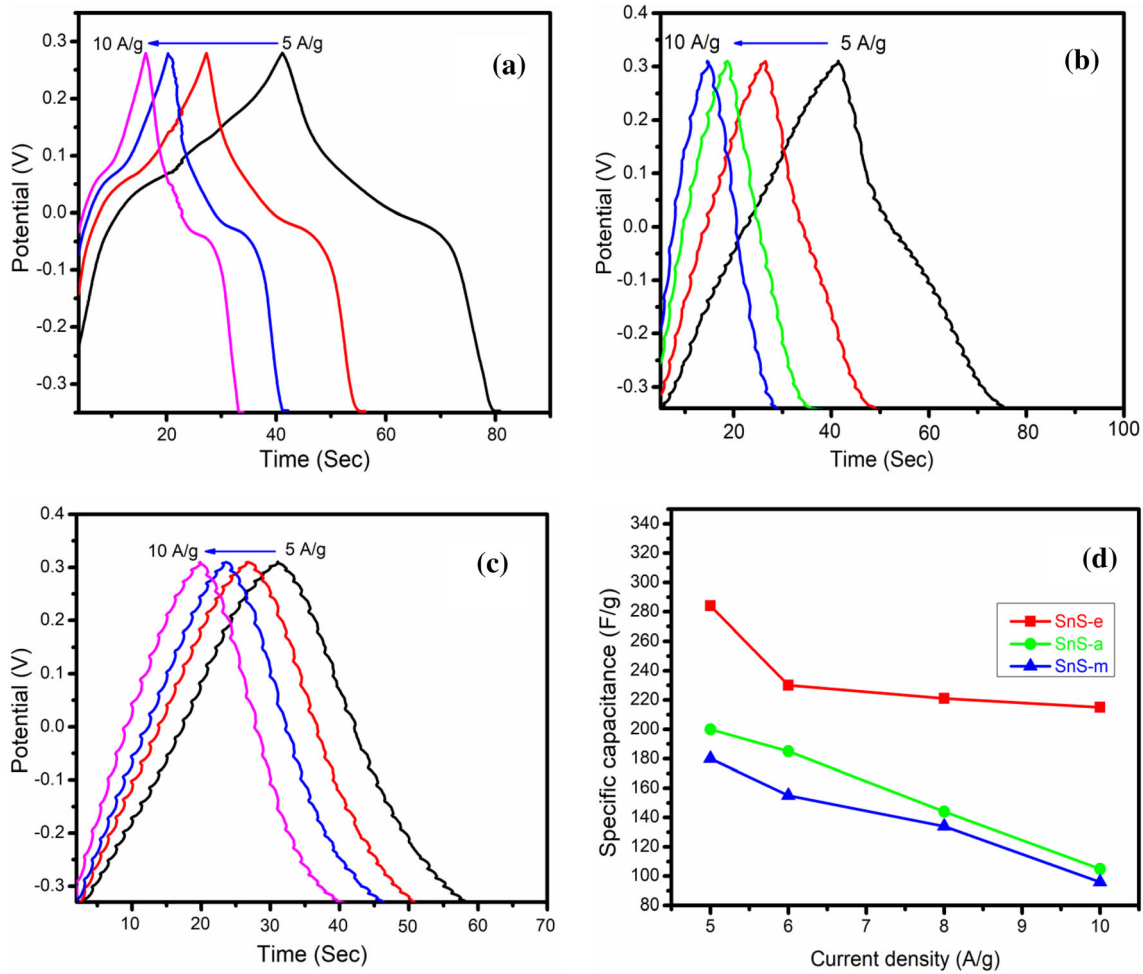


Fig. 12 a–c GCD curves d Variation of current density with specific capacitance of SnS-e, SnS-a, and SnS-m electrodes

kg for SnS-a electrode and 180 Wh/kg, 160 Wh/kg, 144 Wh/kg, and 130 Wh/kg for SnS-m electrode, respectively. The corresponding power densities values are 1.6 KWh/kg, 1.9 KWh/kg, 2.6 KWh/kg, and 3.2 KWh/kg for SnS-e electrode; 1.5 KWh/kg, 1.8 KWh/kg, 2.5 KWh/kg, and 3.1 KWh/kg for SnS-a electrode; and 1.4 KWh/kg, 1.7 KWh/kg, 2.4 KWh/kg and 3.0 KWh/kg for SnS-m electrode, respectively. Figure 13 represents the Ragone plot of SnS-e, SnS-a, and SnS-a electrodes indicating SnS-e electrode exhibits the remarkable specific energy density of 216 Wh/kg with the specific power density of 1.6 KWh/kg at a current density of 5 A/g. The columbic efficiency of SnS-e, SnS-a, and SnS-a electrodes can be calculated by using equation [9].

$$\eta = \frac{t_d}{t_c} * 100, \tag{23}$$

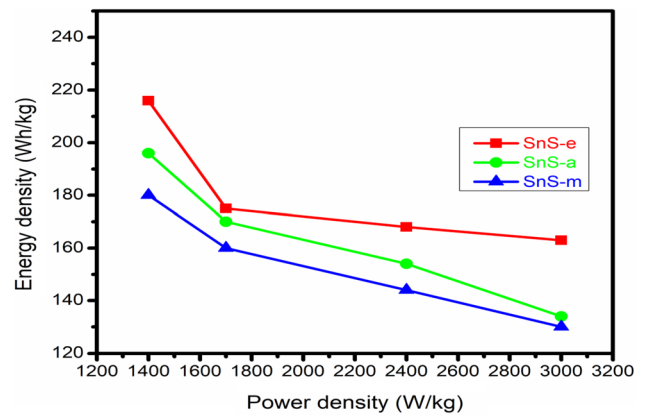


Fig. 13 Ragone plot of SnS-e, SnS-a, and SnS-m electrodes

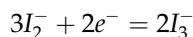
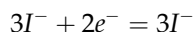
where η is the columbic efficiency, t_d is the discharging time, and t_c is the charging time. The efficiency of SnS-e electrode is 86%, 80%, and 74%, respectively. The values of specific capacitance

calculated by using CV and GCD curves, energy density, power density, and efficiency clearly understand that SnS-e electrodes possess better electrochemical performance compared to the SnS-a and SnS-m electrodes which is due to the less energy gap value and clear spherical morphology as compared to the SnS-a and SnS-m nanoparticles. Also, the specific capacitance of SnS-e electrode is better than the reported work (Table 2).

3.8 Photovoltaic performance

The photo-electrochemical measurements of SnS-e, SnS-a, and SnS-m electrodes were examined in a three-electrode electrochemical workstation (CH Instruments, USA) using UV-Vis light (Xenon lamp) as a source. The CEs of Pt, SnS-e, SnS-a, SnS-m of DSSCs were reflected by J-V curves under one sun illumination (AM 1.5 G, 100 mW cm⁻²). The electrocatalytic activity of Pt, SnS-e, SnS-a, and SnS-m CEs was evaluated by CV measurement with the scanning potential that varied from -0.6 to 0.3 V at constant scan rate of 50 mV s⁻¹. The prepared electrolyte was composed of 10.0 m M LiI, 1.0 mM I₂, and 0.1 M LiClO₄ in anhydrous acetonitrile. For Tafel polarization curve measurement, asymmetrical dummy cell was assembled based on the liquid electrolytes for the CEs and measured at a scanning rate of 10 mV s⁻¹. Figure 14a shows the cyclic voltammograms of Pt, SnS-e, SnS-a, and SnS-m CEs. All these CV curves show two pairs of oxidation and

reduction peaks and can be described by the following equations [50]:



The relative positive pair is attributed to the oxidation and reduction of $\frac{I_2}{I_3^-}$, whereas the relative negative pair is attributed to the oxidation and reduction of $\frac{I_3^-}{I_2^-}$. The CV profile and peak positions of SnS-m, SnS-a, SnS-e, and Pt CEs are similar to each other, indicating that SnS-m, SnS-a, and SnS-e CEs are effective in catalyzing the reduction of tri-iodide to iodide and possess better catalytic activity.

Tafel polarization curves of pt, SnS-e, SnS-a, and SnS-m CEs are as shown in Fig. 14b and it is clearly observed that the exchange current density and limiting diffusion current density parameters in the Tafel polarization curves have the same sequence ratios of respective electrodes. It can be seen that SnS-e electrode exhibits the strong charge transfer ability and diffusion ability than the other CEs indicating high electrocatalytic activity for the I⁻/I₃⁻ redox couple. Thus, these results are coincide with the CV results.

The effects of Pt, SnS-e, SnS-a, and SnS-m CEs on the photovoltaic performance of DSSCs is systematically investigated and the resulting J-V curves are shown in Fig. 15. The obtained DSSCs Photovoltaic parameters such as open-circuit voltage (V_{oc}), short-circuit current density (J_{sc}), fill factor (FF), and photoconversion efficiency (PCE) are calculated using the

Table 2 Comparison of the Specific capacitance of SnS-e, SnS-a, and SnS-m electrodes with the literature reports

Method	Electrode	Electrolyte	Specific capacitance F/g	References
Solvothermal	SnS-e	3 M KOH	2463	Present work
	SnS-a		1249	
	SnS-m		749	
Chemical precipitation	SnS	6 M KOH	545	[46]
	SnS/G		980	
Hydrothermal	SnS	1 M KOH	201	[47]
Solvothermal	SnS	2 M Na ₂ So ₄	70	[9]
Chemical Precipitation	SnS	0.1 M KOH	19.25	[48]
	SnS/C		36.16	
Hydrothermal	SnS	0.1 M KOH	6.19	[49]
		0.1 M NaCl	4.19	

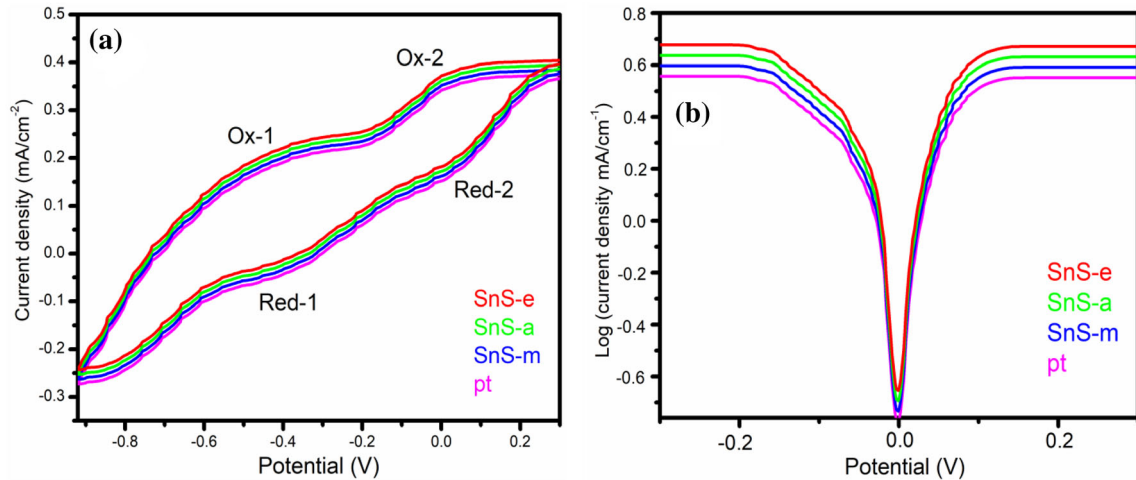


Fig. 14 **a** CV curves of SnS-e, SnS-a, SnS-m, and pt CEs. **b** Tafel polarization curves SnS-e, SnS-a, SnS-m, and pt CEs (Color figure online)

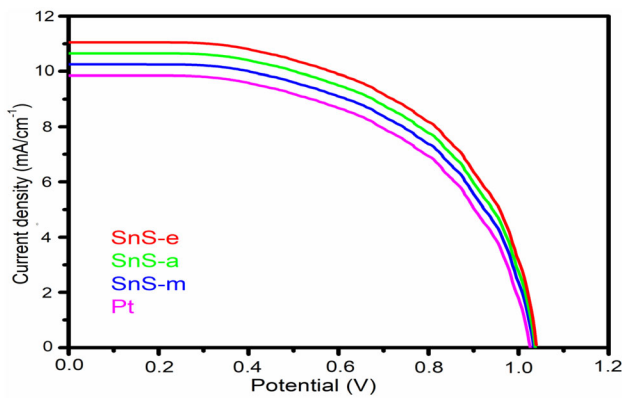


Fig. 15 J–V curves of DSSCs based on SnS-e, SnS-a, SnS-m, and pt CEs (Color figure online)

following equation and the results are presented in Table 3. [51]

$$FF = \frac{I_{max} V_{max}}{I_{sc} V_{sc}} \tag{24}$$

Table 3 Photovoltaic parameters of Pt to SnS-e, SnS-a, and SnS-m CEs

CE	J_{sc} (mA cm ⁻²)	V_{oc} (V)	FF	PCE (%)
Pt	8	0.7	0.56	9.80
SnS-m	8.4	0.72	0.57	9.86
SnS-a	8.8	0.75	0.59	9.90
SnS-e	9.1	0.78	0.60	9.99

$$\eta(\%) = \frac{I_{sc} V_{oc}}{P_{in}} * FF * 100, \tag{25}$$

where ‘FF’ is the fill factor, ‘η’ is the photoconversion efficiency, ‘I_{max}’ is the maximum current density, ‘V_{max}’ is the maximum voltage, ‘I_{sc}’ is the short-circuit current density, and ‘V_{oc}’ is the open-circuit potential. The ‘P_{in}’ is input power in watt/cm² which is equal to I_{max}V_{max}.

From the J–V measurement, the I_{sc} from Pt electrode to SnS-m, SnS-a, and SnS-e was observed to be 8, 8.4, 8.8, and 9.1 mAcm⁻² and the corresponding open-circuit voltage ‘V_{oc}’ were 0.7, 0.72, 0.75, and 0.78 V, respectively. The photoconversion efficiency (η) from platinum electrode to SnS-m, SnS-a, and SnS-e electrodes were 9.80%, 9.86%, 9.90%, and 9.99%, respectively. From these observations, it is clear that

Table 4 Comparison of photoconversion efficiency of SnS CEs with literature reports

Material	photoanode	CEs	Efficiency (%)	References
SnS-e	TiO ₂	Pt	9.99	Present work
SnS-a			9.90	
SnS-m			9.86	
SnS-NSs	TiO ₂	Pt	6.16	[50]
SnS-NWs			5.00	
SnS films	TiO ₂	Pt	2.00	[52]
SnS QDs	TiO ₂	Pu	0.326	[53]
SnS	TiO ₂	Au	0.010	[54]
SnS QDs	TiO ₂	Pt	0.072	[55]

the nanospherical morphology facilitates increased light absorbing ability than 1D nanostructured TiO₂ nanorods [52]. Moreover, from the calculated values of J–V parameters and comparing the photoconversion efficiency of SnS-e with the literature reports (Table 4), it is clearly observed that SnS-e possesses better photovoltaic performance than SnS-a, SnS-m, and Pt CEs, respectively.

4 Conclusion

In this study, three different SnS nanostructures were synthesized by using cheap and easily available solvents through solvothermal method. The energy band gap of 1.1 eV is attained by nanospheres of SnS-e electrode and possesses higher specific capacitance of (2463 F/g) at the Scan rate of 10 mV/s. The DSSCs device with SnS-e nanoparticles as CEs was with highest effective power conversion efficiency of 9.99%, compared to other electrodes. Thus, this study reveals low cost method for synthesization of SnS nanoparticles in ethanol could become a promising material for supercapacitor and CEs alternative to platinum counter electrodes.

References

1. A.P. Alivisatos, *Science* **271**, 933–937 (1996)
2. X. Duan, Y. Huang, R. Agarwal, C.M. Lieber, *Nature* **421**, 241–245 (2003)
3. M.S. Fuhrer, J. Nygard, L. Shih, M. Forero, Y. Young-Gui, M.S.C. Mazzoni, C.H. Joon, *Science* **288**, 494–497 (2000)
4. Z.L. Xiao, C.Y. Han, W.K. Kwok, H.H. Wang, U. Welp, J. Wang, G.W. Crabtree, *J. Am. Chem. Soc.* **126**, 2316–2317 (2004)
5. V.V. Kindyak, N.N. Koren, V.V. Moiseenko, V.F. Gremenok, *Thin Solid Films* **207**, 220–222 (1992)
6. N.K. Reddy, M. Devika, E. Gopal, *Crit. Rev. Solid State Mater. Sci.* **40**, 359–398 (2015)
7. S. Li, J. Zheng, Z. Hu, S. Zuo, Z. Wu, P. Yan, F. Pan, *RSC Adv.* **5**, 72857–72862 (2015)
8. S.S. Hegde, A.G. Kunjomana, M. Prashantha, C. Kumar, K. Ramesh, *Thin Solid Films* **545**, 543–547 (2013)
9. H. Chauhan, M.K. Singh, S.A. Hashmi, S. Deka, *RSC Adv.* **5**, 17228 (2015)
10. Y. Sui, J. Appenzeller, *Nano Lett.* **9**, 2973–2977 (2009)
11. J.H. Kim, K.H. Lee, L.J. Overzet, G.S. Lee, *Nano Lett.* **7**, 2611–2617 (2011)
12. X. Zhao, L. Zhang, S. Murali, M.D. Stoller, Q. Zhang, Y. Zhu, R.S. Ruoff, *ACS Nano* **6**, 5404–5412 (2012)
13. X. Rui, H. Tan, Q. Yan, *Nanoscale* **6**(17), 9889–9924 (2014)
14. H.L. Zhu, D. Yang, H. Zhang, *Mater. Lett.* **60**, 2686–2689 (2006)
15. H. Tang, J.G. Yu, X.F. Zhao, *J. Alloys Compd.* **460**, 513–518 (2008)
16. S. Biswas, S. Kar, S. Chaudhuri, *Appl. Surf. Sci.* **253**, 9259–9266 (2007)
17. C.H. An, K.B. Tang, G.Z. Shen, C.R. Wang, Q. Yang, B. Hai, Y.T. Qian, *J. Cryst. Growth* **244**, 333–338 (2002)
18. Q.-S. Jiang, W. Li, J. Wu, W. Cheng, J. Zhu, Z.Q. Yan, X. Wang, Y. Fen, *J. Mater. Sci.* **30**, 9429–9437 (2019)
19. M. Salavati-Niasaria, D. Ghanbaria, F. Davar, *J. Alloys Compd.* **492**, 570–575 (2010)
20. D. Nath, F. Singh, R. Das, *Mater. Chem. Phys.* **239**, 122021 (2020)
21. R. Yogamalar, R. Srinivasan, A. Vinu, K. Ariga, A.C. Bose, *Solid State Commun.* **149**, 1919–1923 (2009)
22. A.K. Zak, W.H.A. Majid, M.E. Abrishami, R. Yousefi, *Solid State Sci.* **13**, 251e256 (2011)
23. D.B. Cullity, *Elements of X-Ray Diffraction* (Addison-Wesley Publishing Co., Inc., Reading, MA, 1956)
24. G.K. Williamson, R.E. Smallman, *Philos. Mag.* **1**(1), 34–35 (1956)
25. K.M. Batoor, E.H. Raslan, Y. Yang, S.F. Adil, M. Khan, A. Imran, Y. Aldouri, *AIP Adv.* **9**, 055202 (2019)
26. M. N. Ashiqqa, S. Irshad, M. F. Ehsanb, S. Rehmana, S. Farooq, M. Najam-Ul-Haq, A. Ziab, N. J. Chem. (2017), 1–23.
27. B.E. Warren, B.L. Averbach, *J. Appl. Phys.* **23**(4), 497 (1952)
28. D. Balzar, H. Ledbetter, *J. Appl. Crystallogr.* **26**(1), 97–103 (1993)
29. W.H. Hall, X-ray line broadening in metals. *Proc. Phys. Soc. Sect. A* **62**(11), 741–743 (1949)
30. M.A. Tagliente, M. Massaro, *Methods Phys. Res. B.* **266**(7), 1055 (2008)
31. M. Li, Y. Wu, T. Li, Y. Chen, H. Ding, Y. Lin, N. Pan, X. Wang, *RSC Adv.* **7**, 48759–48765 (2017)
32. X.L. Gou, J. Chen, P.W. Shen, *Mater. Chem. Phys.* **93**, 557–566 (2005)
33. T. Radik, M. Grossberg, J. Raudoja, R. Traksmaa, J. Krustok, *J. Phys. Chem. Solids* **74**, 1683–1685 (2013)
34. M. Parenteau, C. Carlone, *Phys. Rev. B* **41**, 5227 (1990)
35. J. Henry, K. Mohanraj, S. Kannan, S. Barathan, G. Sivakumar, *Eur. Phys. J. Appl. Phys* **61**, 10301–10304 (2013)
36. C.Y. Panicker, H.T. Varghese, D. Philip, *Spectrochim. Acta Part A* **65**, 802–804 (2006)

37. L.K. Khel, S. Khan, M.I. Zaman, J. Chem. Soc. Pak. **27**, 24–28 (2005)
38. J. Zai, X. Qian, K. Wang, C. Yu, L. Tao, Y. Xiao, J. Chen, CrystEngComm **14**, 1364–1375 (2012)
39. J. Grau, M. Akinc, J. Am. Ceram. Soc. **80**, 941–951 (1997)
40. E.A. Butler, D.G. Peters, E.H. Swift, Anal. Chem. **30**, 1379–1383 (1958)
41. P. Asen, M. Haghghi, S. Shahrokhian, N. Taghavinia, J. Alloys Compd. **782**, 38–50 (2019)
42. G.S. Gund, D.P. Dubal, S.B. Jambure, S.S. Shinde, C.D. Lokhande, J. Mater. Chem. A **1**, 4793–4803 (2013)
43. A.M. Patil, A.C. Lokhande, P.A. Shinde, H.D. Shelke, C.D. Lokhande, Int. J. Eng. **10**(1), 974–912 (2017)
44. K. Deori, S.K. Ujjain, R.K. Sharma, S. Deka, A.C.S. Appl. Mater. Interfaces **5**, 10665 (2013)
45. F. Beguin, E. Frackowiak, *Supercapacitors: Materials, Systems and Applications* (Wiley, New York, 2013)
46. S. Ravuri, C.A. Pandey, R. Ramchandran, S.K. Jeon, A.N. Grace, Int. J. Nanosci. **16**, 1760022 (2017)
47. R. Barik, N. Devi, V.K. Perla, S.K. Ghosh, K. Mallick, Appl. Surf. Sci. **18**(30858–6), 4 (2018)
48. Y. Li, H. Xie, J. Tu, Nanostructured SnS/carbon composite for supercapacitor. Mater. Lett. **63**, 1785–1787 (2009)
49. M. Jayalakshmi, M.M. Rao, B. Choudary, Electrochem. Commun. **6**, 1119–1122 (2004)
50. F. Alam, V. Dutta, Appl. Surf. Sci. xxx (2015) xxx–xxx
51. J.P. Sawant, R.B. Kale, J. Solid State Electrochem. **24**, 461–472 (2020)
52. X. Chen, Y. Hou, B. Zhang, X.H. Yang, H.G. Yang, Chem. Commun. **49**(51), 5793–5795 (2013)
53. Y. Zhao, H. Pan, Y. Lou, X. Qiu, J. Zhu, C. Burda, J. Am. Chem. Soc. **131**, 4253–4261 (2009)
54. Y.B. Chen, L. Chen, L.M. Wu, Chem. Eur. J. **14**, 11069–11075 (2008)
55. N. Spalatu, J. Hiie, R. Kaupmees, O. Volobujeva, J. Krustok, A.I. Oja, M. Krunks, ACS Appl. Mater. **11**, 17539–17554 (2019)

Publisher's Note Springer Nature remains neutral with regard to jurisdictional claims in published maps and institutional affiliations.